npj | flexible electronics

Article

Published in partnership with Nanjing Tech University

Article in Press

https://doi.org/10.1038/s41528-026-00637-2

Predictable conformal electronics enabled by a sliding-adhesion competition model

Qixuan Zhu[1,2], Jinshuai Sun[1], Huihui Ma[1], Yue Wei[1], Zhengyang Zhou[1], Miao Lei[1], Zhiyuan Wang[1], Zihan Hao[1], Yifu Lei[1], Xueqian Yang[1], Zihao Xu[1], Yuan Wei[3], Xiaoxu Wang[2] ✉, Xuewen Wang[1] ✉, Zhaohe Dai[4], Wei Huang[1] ✉ & Qianbo Lu[1,5] ✉

Achieving conformal attachment between flexible electronics and complex curved surfaces remains a fundamental challenge, as existing predictive methods are either computationally intensive or lack generality across arbitrary geometries. Here, we introduce a sliding-adhesion competition conformal model (SAM) based on differential geometry, which enables efficient and accurate prediction of conformability for arbitrary shape-surface mappings. By formulating a conformal factor derived from the first fundamental form of surfaces and incorporating interfacial adhesion and friction effect, SAM quantifies strain distributions and provides reliable failure predictions across diverse surfaces, while improving computational efficiency by 3–4 orders of magnitude compared to finite element analysis. Furthermore, the model offers the first quantitative insight into the superior conformability of high-aspect-ratio serpentine structures and supports high-precision inverse design of functional patterns such as antennas and sensor arrays, reducing placement errors to below 3%. SAM establishes a universal and scalable framework for the conformal integration of flexible electronics, with broad applicability in biomedical, aerospace, and soft robotic systems.

Flexible electronics technology is reshaping the frontiers of human-machine interaction and bio-adhesive devices, encompassing curved displays[1,2], wearable sensing systems[3–5], microneedle patches[6,7], organ/tissue monitoring devices[8–10], smart skins[11,12], and conformal antennas[13,14]. A core challenge in this domain is achieving conformal attachment of electronic devices to complex surfaces. In recent years, the prediction of conformability for target surface attachment and the design of conformal structures have emerged as critical concerns in research related to electronic skins, smart skins, and soft robotics[15,16].

When flexible electronic devices are attached to curved surfaces, non-uniform strain distributions can occur due to deformation[17], which in turn impairs the structural integrity and functional stability of the devices[18]. To achieve conformal attachment between devices and surfaces, existing studies have pursued two primary strategies. First is enhancing the mechanical adaptability of devices to surface deformation. This approach involves both material and structural design. For materials, research focuses on developing stretchable polymer materials[19–22] and liquid-phase materials[23,24] to accommodate large deformations. For structures, engineered architectures such as buckled structures[25–27], serpentine patterns[28,29], and kirigami structures[30–32] are adopted to dissipate strain energy and prevent device failure under deformation. Second is strengthening the interface bonding between flexible electronics and curved surfaces. This strategy aims to realize stable and reliable conformal attachment through interface engineering, including interfacial adhesion (e.g., material self-adhesion[33–35], chemical adhesives[36–38], and dry adhesion structures[39,40]) and mechanical fixation (e.g., bonding sites[41,42] and mounting structures[43,44]). Despite significant progress in material-structure design and attachment methods, the quantitative relationship between stretchability and conformability remains elusive, which challenges the achievement of conformal attachment of arbitrary device shapes with curved surfaces[45].

[1]State Key Laboratory of Flexible Electronics (LoFE) and Institute of Flexible Electronics (IFE), MIIT Key Laboratory of Flexible Electronics (KLoFE), Shaanxi Key Laboratory of Flexible Electronics, Northwestern Polytechnical University, Xi'an, China. [2]School of Automation, Northwestern Polytechnical University, Xi'an, China. [3]The Institute of Future Agriculture (IFA), Northwest A&F University, Xianyang, China. [4]Department of Mechanics and Engineering Science, State Key Laboratory for Turbulence and Complex Systems, College of Engineering, Peking University, Beijing, China. [5]Key Laboratory of Flexible Electronics of Zhejiang Province, Ningbo Institute of Northwestern Polytechnical University, Ningbo, China. ✉e-mail: woyaofly1982@nwpu.edu.cn; iamxwwang@nwpu.edu.cn; vc@nwpu.edu.cn; iamqlu@nwpu.edu.cn

Conformability is governed by multiple factors, including shape-surface strain distribution, the mechanical properties of flexible electronic devices, and interfacial adhesion energy[15]. Rogers et al. employed finite element analysis (FEA) to quantify these factors[9,26,27] and further conducted conformal design by Zhang et al.[41,46] though this approach entails substantial computational cost. In contrast, some researchers have proposed semi-analytical models that improve computational efficiency, although they are largely restricted to specific curved surfaces (e.g., spherical surfaces)[47,48], which limits their general applicability to diverse shape-surface mappings and attachment configurations. Meanwhile, the differential geometry[49] and computer graphics[50] techniques have been introduced to support flexible conformal design while often overlooking the roles of mechanical properties and interfacial energy in determining conformability. The buckling, delamination, and fracture of thin devices result in a good deal of complexity that precludes the development of a unified predictive model for conformability that lags behind application needs.

To address this gap, we developed a sliding-adhesion competition conformal model (SAM) grounded in the first fundamental form of differential geometry. This model enables accurate and rapid conformability analysis for arbitrary shape-surface mappings, showing full agreement with four repeated failure tests and improving analysis efficiency by 3–4 orders of magnitude compared to FEA methods. We further validated the model through conformal design experiments on specific curved surfaces, including cardiac tissues and aircraft models, where designs based on the SAM improved precision by nearly an order of magnitude over blank control groups. The proposed model offers an efficient and versatile tool for conformability prediction in flexible electronics, with the potential to extend the application boundaries of such devices in areas such as robotic skins, soft actuators, and implantable sensor systems.

Results

Sliding-adhesion competition conformal model for arbitrary shape-surface mappings analysis

As illustrated in Fig. 1a, we define conformal attachment based on the geometric deformation of a flexible device before and after attachment: a device with a specific initial shape conforms to a target region on a target surface such that its final shape matches the target shape. Herein, the "initial shape" refers to the stress-free pattern of the device before attachment, idealized as a surface with defined boundaries under negligible bending stiffness. Commonly studied initial shapes include circles[4], rectangles[10,19,51], line-type[8,28,52], and other kirigami patterns[9,30,53]; they can also be processed into three-dimensional (3D) architectures via specialized fabrication[54]. The "target surface"[41,47] denotes the surface to which the device is attached, such as mechanical equipment[11,12], human skin[3,5], or internal organs[10,55]. The target surface can be represented analytically[48], numerically as a free-form surface[56], or as a mesh model[50]. The "target shape" refers to a specific region with defined boundaries on the target surface. Figure 1b illustrates the conformal attachment from the initial to the target shape.

To predict conformability, a differential geometry metric is essential. Although Gaussian curvature is often used to characterize surface bending[47–49], it does not directly quantify local length changes during deformation, which is critical for strain analysis. Therefore, we turn to the first fundamental form (FFF, Table 1), I, which provides a complete local description of metric distortion[57].

$$I = Edu^2 + 2Fdudv + Gdv^2 \tag{1}$$

Here, the coefficients E, F, and G are referred to as the first fundamental coefficients, with u and v denoting two parametric directions of a surface. The FFF defines the squared arc length element on a surface (see "Methods"), and inherently encodes information about surface area[48], contact area fraction[47], Gaussian curvature[57], and the Gauss-Bonnet theorem[49]. By comparing the FFFs of the initial and target surfaces, we can derive a "conformal factor" f_c that directly measures the local stretching or compression required for attachment, enabling a quantitative strain analysis for arbitrary shape-surface mappings:

$$f_c = \frac{I_t}{I_i} \tag{2}$$

Here, I_i and I_t represent the FFFs of the initial and target surfaces, respectively, as shown in Fig. 1c. When the conformal factor is not equal to 1, differential geometry dictates that no length-preserving conformal mapping exists locally between the initial and target shapes. Thus, local stretching or compression is inevitable when conforming the device to an arbitrary target region.

The conformal factor enables accurate prediction of the strain distribution after attachment. Adhesion and friction at the interface can lead to complex strain profiles[17]. Inspired by the stick-slip effect[58], we established a sliding-adhesion competition conformal model (SAM, Supplementary Figs. S1–S3). The model analyzes strain by computing the equivalent elongation λ[59]. Let $\lambda^{SLID.}$ And $\lambda^{ADH.}$ denote strain distributions under negligible and the strongest interfacial adhesion and friction, respectively. In practice, the interfacial interaction always falls between these two extreme cases. Therefore, using the squeeze theorem, the elongation λ_u along a parameter direction u can be expressed as a weighted combination of $\lambda^{SLID.}$ And $\lambda^{ADH.}$, given by:

$$\begin{aligned} \lambda^{SLID.} &= \overline{\sqrt{f_c}} = \frac{\int \sqrt{I_t}du}{\int \sqrt{I_i}du} \\ \lambda^{ADH.} &= \sqrt{f_c} = \sqrt{\frac{I_t}{I_i}} \\ \lambda_u &= \alpha\lambda^{SLID.} + \beta\lambda^{ADH.} \end{aligned} \tag{3}$$

Herein, α and β denote the sliding and adhesion coefficients, with the constraint $\alpha + \beta = 1.0$ (where $\alpha, \beta \in [0.0, 1.0]$). Their values depend on interfacial interactions. The recommended values for different target surfaces and the corresponding calibration processes are provided in Table S1 and Supplementary Fig. S4. It is important to note that the SAM framework is based on the steady-state analysis of two extreme bounding conditions, making it specifically tailored for low-speed, quasi-static attachment scenarios[60] where inertial effects are negligible. Additionally, this framework mainly targets in-plane deformation analysis of thin films on curved surfaces and thus may not apply to solution-based coating strategies[61] or assessments of through-thickness structural bending failures[62] (Supplementary Fig. S5).

As illustrated in Fig. 1d, typical outcomes of conformal attachment include compliance and failure of compression, adhesion, yielding, and fracture. We identify three governing factors for conformability based on prior work[15,45,47,63]:

1. The strain distribution after the initial shape is conformally attached to the target shape;

2. The mechanical properties of the device, including yield strain[64], elongation at break[65], and compressibility[66];

3. The interfacial adhesion energy $E_{adh.}$[67,68].

Using these quantities, we predict conformability and failure modes as follows. From λ_u and λ_v from two parameter directions u and v, we compute the equivalent strain energy $E_{stra.}(u, v)$ and equivalent elongation $\lambda(u, v)$ (Supplementary Note 1). These are compared against the material's mechanical thresholds, including yield strain energy $E_{yiel.}$ And elongation $\lambda_{yiel.}$ (Where $\lambda_{yiel.} = \varepsilon_{yiel.} + 1$ and $\varepsilon_{yiel.}$ is the yield strain), fracture energy $E_{frac.}$ And elongation $\lambda_{frac.}$, and compressible energy $E_{comp.}$ and elongation $\lambda_{comp.}$ (where $\lambda_{comp.} = \varepsilon_{comp.}+1$ and $\varepsilon_{comp.}$ is the compressible strain), along with the adhesion energy $E_{adh.}$ and elongation $\lambda_{adh.}$. As depicted in Fig. 1e,

If $E_{stra.} \geq E_{frac.}$ (or $\lambda \geq \lambda_{frac.}$), the device fractures (red);

If $E_{yiel.} \leq E_{stra.} < E_{frac.}$ (or $\lambda_{yiel.} \leq \lambda < \lambda_{frac.}$), it yields (orange);

If $E_{comp.} \leq E_{stra.} < E_{yiel.}$ And $E_{adh.} < |E_{stra.}|$ (or $\lambda_{comp.} \leq \lambda < \lambda_{yiel.}$ and $\lambda < \lambda_{adh.}$), adhesion failure arises (yellow);

If $E_{stra.} < E_{comp.}$ (or $\lambda < \lambda_{comp.}$), compression failure occurs (purple);

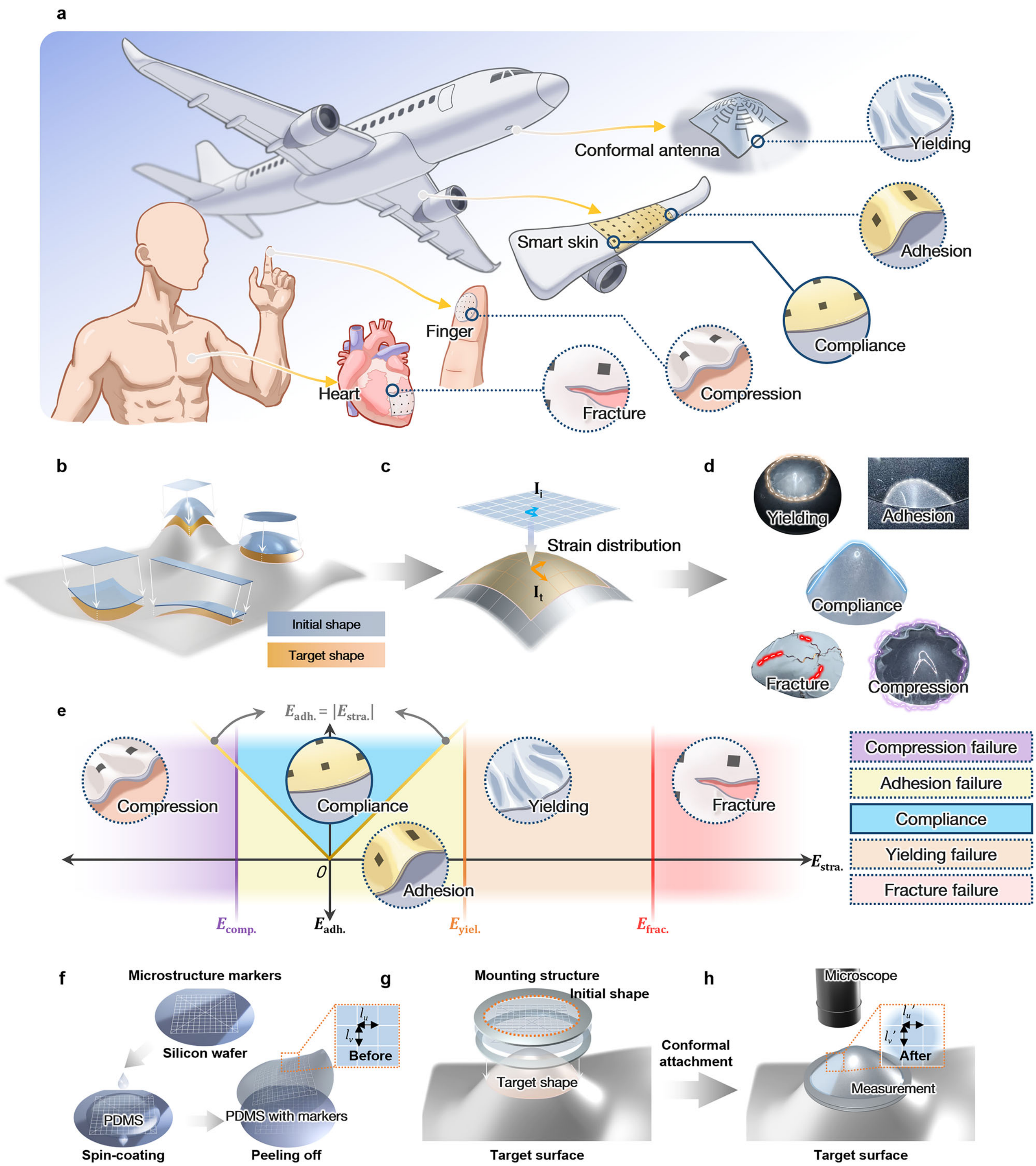

Fig. 1 | Analysis and prediction for conformal attachment of flexible devices. **a** Representative scenarios of conformal attachment for flexible devices, including cardiac tissues, human fingers, smart skins, and conformal antennas. **b** Illustration of conformal attachment for arbitrary shape-surface mappings. **c** Accurate calculation of strain distribution using the sliding-adhesion competition conformal model. **d** Compliance and distinct failure modes of conformal attachment. **e** Definition and prediction of compliance and distinct failure modes of conformal attachment using the sliding-adhesion competition conformal model. **f** Fabrication of marker-patterned PDMS film on silicon wafer. **g** Conformal attachment of PDMS film onto the target surface. **h** Microscopic scanning measurement of deformed markers to obtain strain distributions.

Only if $E_{comp.} \leq E_{stra.} < E_{yiel.}$ and $E_{adh.} \geq |E_{stra.}|$ (or $\lambda_{comp.} \leq \lambda < \lambda_{yiel.}$ and $\lambda \geq \lambda_{adh.}$), compliance is achieved (blue).

The SAM thus provides a quantitative definition and prediction for the conformability across arbitrary geometries and material systems. Note that the failure modes we define exhibit correlations with commonly used failure classifications such as buckling and delamination, yet they are distinct. Conventional classifications are predominantly descriptive of outward manifestations, whereas our proposed failure modes are based on energy and strain-based mechanistic criteria.

To rigorously evaluate the predictive capabilities of the SAM framework against physical reality, we established a systematic hardware testing and characterization pipeline, with the overall experimental workflow

Table 1 | Notations of key variables and parameters

Variable/parameter	Notation
First fundamental form (FFF)	I
FFF of the target shape surface	I_t
FFF of the initial shape surface	I_i
Conformal factor	f_c
Strain energy	$E_{stra.}$
Maximum compressive energy	$E_{comp.}$
Yield strain energy	$E_{yiel.}$
Fracture strain energy	$E_{frac.}$
Adhesion energy	$E_{adh.}$
Equivalent elongation	λ
Compressible elongation	$\lambda_{comp.}$
Yield strain	$\varepsilon_{yiel.}$
Yield elongation	$\lambda_{yiel.}$
Elongation at break	$\lambda_{frac.}$
Compressibility strain	$\varepsilon_{comp.}$
Adhesion elongation	$\lambda_{adh.}$
Coefficient of sliding term	α
Coefficient of adhesion term	β
Elongation with negligible adhesion and friction effect	$\lambda^{SLID.}$
Elongation with the strongest adhesion and friction effect	$\lambda^{ADH.}$
Spherical surface	S_s
Ellipsoid surface	S_e
Paraboloidal surface	S_p
Trigonometric surface	S_t
Free-form surface	S_f

schematically illustrated in Fig. 1f–h. First, microstructural markers (l_u, l_v) are fabricated on silicon wafers via standard Micro-electro-mechanical systems processes. A Polydimethylsiloxane (PDMS) precursor solution is subsequently spin-coated onto the wafer to form a PDMS film patterned with these markers (Fig. 1f). The as-prepared film is clamped by the mounting structure (a pair of gaskets) to preserve its initial shape and conformally attached onto the target shape region of the target surface (Fig. 1g) on a custom platform (see "Method" for Conformal attachment platform and Supplementary Fig. S7). Finally, microscopic scanning measurements (l_u', l_v') on the marker dimensions are performed to extract the full strain distribution (see Fig. 1h, "Methods" for Strain distribution measurement, and Supplementary Fig. S8). Additionally, marker patterns with distinct initial geometries enable diverse parametric design. The experimentally measured boundary strain profiles and failure morphologies are subsequently used to benchmark the predictions from the SAM framework and FEA results across various shape–surface combinations.

Conformability analysis and prediction on analytical surfaces

We first validate the SAM using analytical surfaces, the simplest class of target surfaces[46], with a spherical surface as a canonical example. As shown in Fig. 2a, the target surfaces were set to four types of analytical surfaces with non-zero Gaussian curvature K_g, including spherical, ellipsoid, paraboloidal, and trigonometric surfaces (expressions and photographs in Supplementary Table S2 and Fig. S6). The initial shape was designed as a circular planar shape with diameter D. The boundary of the target shapes corresponded to the projection boundary of the circle onto the target surfaces along the z-axis direction.

With precise attachment realized on the custom platform, repeated measurements of strain distributions were performed using micro-markers and microscopic imaging (see raw six replicates per group in Supplementary Data S1). PDMS was chosen as the substrate material[3,4,6,7], with a maximum compressibility $\lambda_{comp.} = 1.00$, approximately equal yield and fracture strain energies, and a fracture elongation $\lambda_{frac.} = 2.00$. Equivalent elongation $\lambda(u)$ was computed using the SAM, yielding equivalent elongations $\lambda_s(u)$, $\lambda_e(u)$, $\lambda_p(u)$, and $\lambda_t(u)$ for each surface (Supplementary Note 2, Table S3, and Table S4). Herein, $\lambda(u, v)$ was reduced to $\lambda(u)$ in terms of the rotational symmetry, with v held constant and $u \in [0, D]$. Conformability was assessed as follows: compression failure occurs when $\lambda_{min} < 1.00$, and fracture failure occurs when $\lambda_{max} > 2.00$, where λ_{min} and λ_{max} denote the minimum and maximum values of $\lambda(u)$.

For a circular initial shape ($D = 10$ mm) on a spherical surface ($R = 14$ mm), as shown in Fig. 2b, SAM predicted $\lambda_{min} = 1.02$ (larger than 1.00, means no compression) and $\lambda_{max} = 1.20$ (smaller than $\lambda_{frac.}$, means no fracture), in close agreement with FEA (1.03, 1.23, $R^2 = 0.89$) and experiment (1.02, 1.23, $R^2 = 0.93$). As shown in the subplot in Fig. 2b, λ_{max} increases with D at fixed Gaussian curvature K_g, and with K_g at fixed D. When D increased to 14 mm, SAM predicted $\lambda_{max} = 3.33$ at the boundary, and λ_{min} remained larger than 1.00, indicating fracture failure. Experiments confirmed circular fracture along the boundary, consistent with the surface's rotational symmetry (Fig. 2c). SAM shows excellent consistency with FEA, with $R^2 = 0.99$, with a computational time of 0.045 s, which is three orders of magnitude faster than the FEA (20 s). This speedup is highly beneficial for applications such as pattern optimization in conformal design.

Similarly, for $D = 10$ mm on ellipsoid, paraboloidal, and trigonometric surfaces, as shown in Fig. 2d, 2f, and 2h, SAM gave (λ_{min}, λ_{max}) values of (1.08, 1.39), (1.16, 1.64), and (1.22, 1.76), respectively. All $\lambda_{min} > 1.00$ and $\lambda_{max} < 2.00$ indicated successful conformal attachment without failure, corroborated by FEA and experiments with the minimum R^2 value of 0.94. (Table 2, Supplementary Movie 1, Supplementary Tables S5 and S6).

Subplots in Fig. 2d, f, h show that λ_{max} increases with D and K_g for all surfaces. At $D = 14$ mm and high K_g, λ_{max} exceeded 2.00 in all three cases shown in Fig. 2e, g, i, correctly predicting fracture along approximately circular boundaries, as confirmed experimentally (Supplementary Movie 1).

SAM agreed with all four repeated tests (one trial presented in the main manuscript and three replicate tests shown in Supplementary Fig. S9), with computation times under 0.05 s (Supplementary Table S7). It also accurately predicted behavior in critical attachment scenarios (where 90% $\lambda_{frac.} < \lambda_{max} < 100\%\lambda_{frac.}$, e.g., $D = 12$ mm on different analytical surfaces; Supplementary Fig. S10) and critical failure scenarios (where 100% $\lambda_{frac.} < \lambda_{max} < 110\%\lambda_{frac.}$), confirming its high precision. When the substrate material was switched to Ecoflex ($\lambda_{frac.} = 6.00$, with a hardness of Shore 00-50, sourced from Smooth-On, Inc., USA), no fracture occurred for $D = 14$ mm on high-K_g surfaces (Supplementary Fig. S11). In contrast, our model is also applicable to polyvinyl alcohol (PVA) hydrogel and PU (see Supplementary Figs. S12 and S13), for which the relevant calibration may merit consideration where surface energy and friction vary markedly from common low-viscosity material scenarios.

The SAM also enables accurate and efficient prediction of other failure modes in different boundary conditions. For adhesion failure with a free boundary condition, a PET tape with an adhesion elongation limit of $\lambda_{adh.} = 1.02$ was selected. On a spherical surface ($R = 16$ mm), the SAM predicted a maximum elongation λ_{max} of 1.01 at the boundary for a circular device with diameter $D = 3$ mm, indicating successful attachment (Fig. 2j). When D was increased to 4 mm, λ_{max} rose to 1.023, exceeding $\lambda_{adh.}$, and adhesion failure was consequently observed at the boundary (Fig. 2k). For yielding failure, a PET film with a yield elongation of $\lambda_{yiel.} = 1.15$ was used as the conformal material. On a spherical surface ($R = 18$ mm), the SAM obtained λ_{max} values of 1.13 and 1.21 for $D = 10$ mm and $D = 12$ mm, respectively. As predicted, no irreversible yielding took place at the film boundary at $D = 10$ mm (Fig. 2l), while yielding occurs at $D = 12$ mm (Fig. 2m). In addition, the SAM accurately predicted compression failure (Supplementary Fig. S14). This predictive capability is not limited to symmetric configurations, but can be readily extended to arbitrary initial and target boundaries, including more complex conformal attachment configurations.

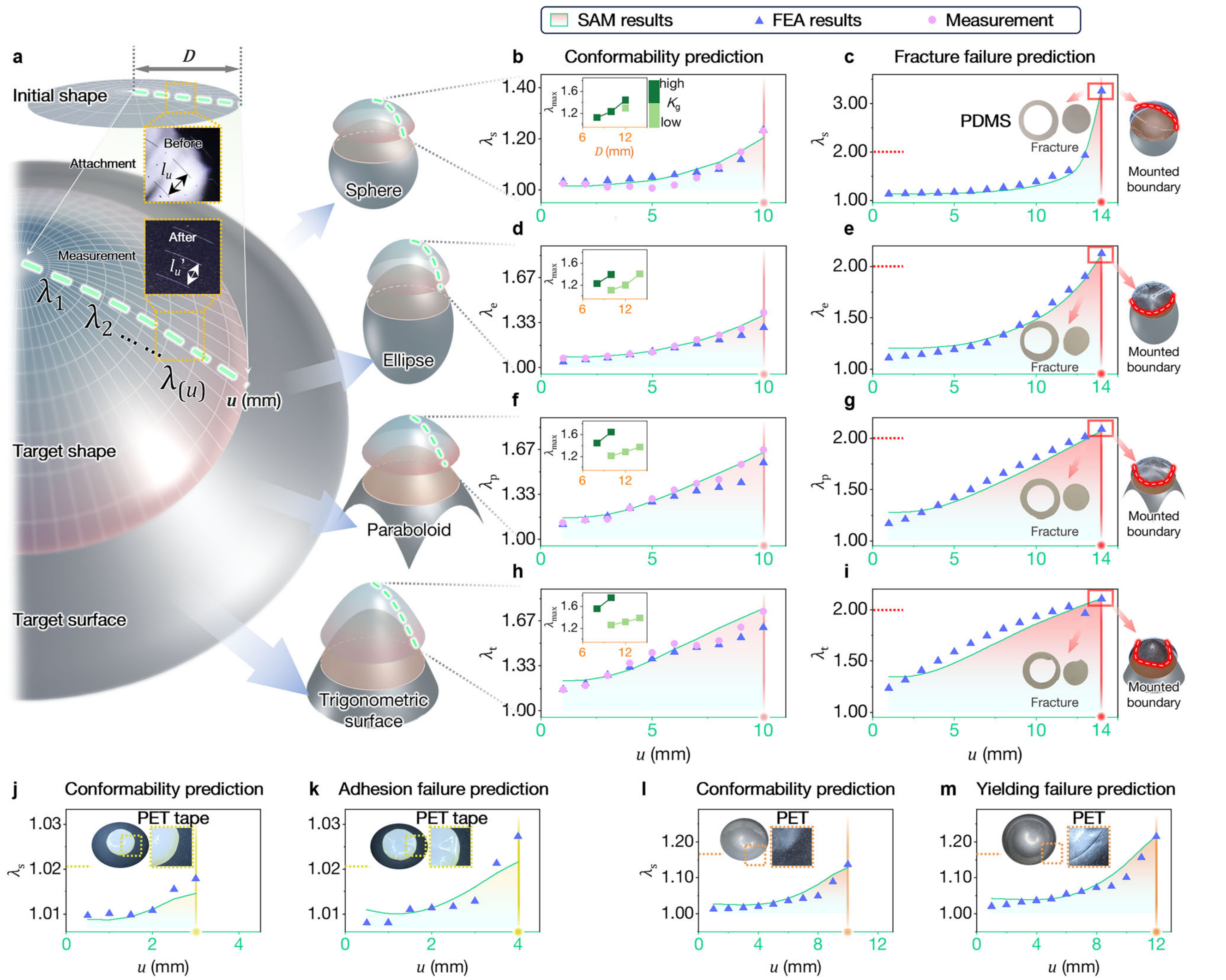

Fig. 2 | Conformability analysis and prediction on analytical surfaces. a Schematic of a circular device conforming to four types of analytical surfaces: spherical, ellipsoid, paraboloidal, and trigonometric. Comparison of predicted and measured elongations versus the parameter direction value u for **b**, **c** spherical, **d**, **e** ellipsoid, **f**, **g** paraboloidal, and **h**, **i** trigonometric surfaces. Results from SAM, FEA, and experiments are plotted for devices of different diameters. The left column represents the case of $D = 10$ mm, and the right column represents the case of $D = 14$ mm. Insets show the dependence of maximum elongation on D and Gaussian curvature K_g. **c**, **e**, **g**, **i** Failure predictions and experimental validation for $D = 14$ mm on each surface type. **j**–**m** Analysis of adhesion failure and yielding failure in critical attachment scenarios. **j** $D = 3$ mm: successful conformal attachment. **k** $D = 4$ mm: boundary adhesion failure. **l** $D = 10$ mm: no irreversible yielding at the film edge. **m** $D = 12$ mm: boundary yielding failure of the PET film.

Table 2 | Comparison of (λ_{min}, λ_{max}) among the results of the SAM, FEA, and measurements

Attachment Pairs		The SAM	FEA	Measurements
Ellipsoid surface	$D = 10$ mm High K_g	(1.08, 1.39)	(1.04, 1.29)	(1.07, 1.41)
Paraboloidal surface	$D = 10$ mm High K_g	(1.16, 1.64)	(1.11, 1.57)	(1.12, 1.66)
Trigonometric surface	$D = 10$ mm High K_g	(1.22, 1.76)	(1.16, 1.62)	(1.16, 1.74)
Free-form surfaces	$L = 18$ mm $z = 20$ mm	(1.00, 1.32)	(1.02, 1.35)	(1.01, 1.28)
	$L = 18$ mm $z = 30$ mm	(1.00, 1.62)	(1.06, 1.60)	(1.04, 1.54)
	$L = 24$ mm $z = 40$ mm	(1.00, 1.62)	(1.05, 1.60)	(1.03, 1.62)

Conformability analysis and prediction on free-form surfaces

Free-form surfaces are complex smooth surfaces defined by control points rather than elementary analytical functions. For conformal attachment experiments, we selected Bézier surfaces[69] as representatives of free-form surfaces. We considered four initial shapes with distinct boundaries: square, rectangular, triangular, and free-curve profiles (Supplementary Fig. S15), as well as four corresponding free-form surfaces (Supplementary Fig. S16). Each Bézier surface was defined using 9 control points (coordinates in Supplementary Table S8). For a given boundary and dimension, a larger z-coordinate of the central control point corresponds to a higher surface curvature. Curvature peaks stay centered for square and rectangular substrates but shift toward the upper v vertex for triangular and free-form boundaries, as reflected by their Gaussian curvature K_g contours in Supplementary Fig. S17. The target

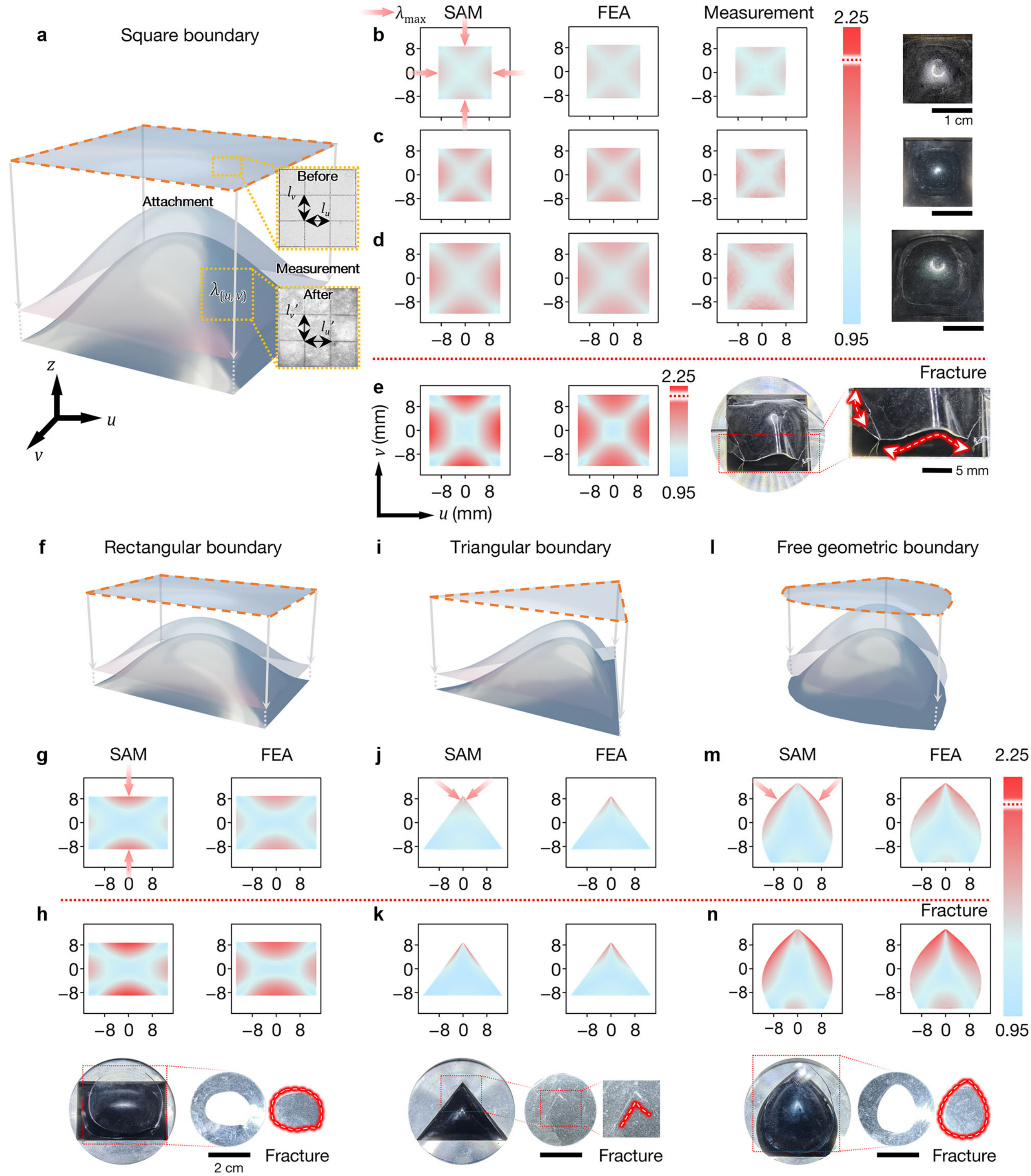

Fig. 3 | Conformability analysis and prediction on free-form surfaces with varied boundaries. a Schematic of a square device attached to a Bézier surface. **b**–**e** SAM-predicted, FEA-simulated, and experimentally measured elongation distributions for square boundaries under increasing central height z and side length L. **b** Square boundary with side length $L = 18$ mm and central control point height $z = 20$ mm. **c** $L = 18$ mm, $z = 30$ mm. **d** $L = 24$ mm, $z = 40$ mm. **e** $L = 24$ mm, $z = 65$ mm and the experimental results of fracture failure. **f**, **i**, **l** Schematic of devices with rectangular, triangular, and free-curve boundaries attached to free-form surfaces. **g**, **h** The SAM, FEA, and experimental results on free-form surfaces with a rectangular boundary: **g** Critical attachment condition $z = 40$ mm. **h** Critical failure condition $z = 50$ mm, and the fracture failure. **j**, **k** The SAM, FEA, and experimental results on free-form surfaces with a triangular boundary: **j** Critical attachment condition $z = 15$ mm. **k** Critical failure condition $z = 18$ mm, and the fracture failure. **m**, **n** The SAM, FEA, and experimental results on free-form surfaces with a free-curve boundary: **m** Critical attachment condition $z = 40$ mm. **n** Critical failure condition $z = 50$ mm, and the fracture failure.

shape was defined as the projection of the initial shape along the z-axis onto the free-form surface. Experimental measurements and SAM implementation for free-form surfaces are detailed in the strain measurement methods, Fig. S18, and Note 3.

Figure 3a presents a schematic illustration of a square initial shape (PDMS substrate) conformally attached to a free-form surface with a square boundary. We analyzed conformability under varying square side lengths (L) and central control point heights (z). Figure 3b–d depict results for

($L = 18$ mm, $z = 20$ mm), ($L = 18$ mm, $z = 30$ mm), and ($L = 24$ mm, $z = 40$ mm), respectively, including SAM, FEA, and experimental results (Raw triplicate measurements per group are listed in Supplementary Data S2) of $\lambda(u, v)$. The maximum elongation consistently occurs near the center of each edge, decreasing toward the corners and the surface center. As summarized in Table 2, all predicted elongation extremes fall between 1.00 and 2.00, with all corresponding R^2 values exceeding 0.90 (see Supplementary Table S6 for full R^2 data). Thus, the model correctly predicts successful conformal attachment without compression or fracture, consistent with experimental observations.

With a further increase in central control point height, the model accurately predicts failure. For $L = 24$ mm and $z = 65$ mm, as illustrated in Fig. 3e, SAM predicted a λ_{max} of 2.25 near the edge midpoints (FEA result is 2.10, $R^2 = 0.92$), exceeding the fracture limit of PDMS ($\lambda_{frac.} = 2.00$). The λ_{min} remained above 1.00, indicating no compression. The predicted edge-initiated fracture is experimentally confirmed in Supplementary Movie 2.

The model generalizes effectively to other boundary types, as validated by four repeated trials (one case plotted in Fig. 3f, i, l, and the other three replicates available in Supplementary Fig. S19), which display rectangular, triangular, and free-curve boundaries, respectively. Under critical attachment conditions, the maximum elongations are 1.95 (rectangle, located at long edge center), 1.92 (triangle, vertex), and 1.94 (free-curve, upper edge), all slightly below $\lambda_{frac.}$, with no compression, as depicted in Fig. 3g, j, m. These results predicted successful critical attachment, which was fully validated by experiments (Supplementary Fig. S20). Under critical failure conditions, as shown in Fig. 3h, k, n, increasing z raises the maximum elongations to 2.29, 2.19, and 2.29, respectively, all exceeding $\lambda_{frac.}$. The SAM results had a high degree of similarity to FEA, with R^2 ranging from 0.86 to 0.95, and experiments validated the fracture predictions. In terms of computational efficiency, the model achieved up to 6000-fold speedup over FEA (Supplementary Table S7). The model maintains high accuracy in repeated tests, including near-threshold scenarios where λ_{max} lies within ±15% of $\lambda_{frac.}$.

Key Observations from Figs. 2 and 3:

(1) SAM accurately predicts conformal behavior on both analytical and free-form surfaces, showing strong agreement with FEA and experiments.

(2) Equivalent elongation scales with the relative dimensions of the initial and target shapes, independent of absolute size, which is consistent with existing findings on spherical surfaces[47,48,58].

(3) The locations of maximum and minimum elongation are shape-dependent. SAM efficiently identifies these extremes, enabling reliable conformability prediction with a 3–4 order-of-magnitude speed advantage over FEA.

Conformability analysis and prediction for line-type shapes

The model also elucidates why line-type, high-aspect-ratio patterns exhibit superior conformability, which is a principle widely adopted in complex surface conformal design[27–29]. Validation experiments were designed as shown in Fig. 4a. A free-form surface defined by 9 control points served as the target surface, with a rectangular boundary of length $L = 27$ mm, width $W = 18$ mm, and central control point height $z = 50$ mm. Initial shapes with aspect ratios of 3:2, 3:1, and 9:1 were tested, transitioning from a near-square to a slender strip. The target shape was defined as the projection of each initial shape onto the surface along the z-axis.

For the initial shape with an aspect ratio of 3:2, SAM predicted a $\lambda_{max} = 2.29$ at the midpoint of the long sides, exceeding $\lambda_{frac.} = 2.00$. Fracture was therefore predicted along the long edges, which was confirmed experimentally (Fig. 4a (i) and Supplementary Movie S2). Increasing the aspect ratio to 3:1 lowered λ_{max} to 1.53, precluding fracture failure. In contrast to the fully fixed boundary condition (Supplementary Fig. S21), pronounced adhesion failure was observed at the midsection of the curved strip when only the two ends were constrained, as shown in Fig. 4a (ii). When the aspect ratio was increased to 6:1, the predicted λ_{max} at the midsection decreased to 1.19, and the conformal attachment behavior became nearly indistinguishable between the two-end fixed and fully fixed boundary conditions (Fig. 4a (iii)). Consequently, for subsequent curved strip patterns with an aspect ratio exceeding 6:1, the boundary condition was simplified to two-end fixation. SAM quantitatively demonstrates that, for a fixed length, increasing the aspect ratio reduces strain along the long axis. For extremely high aspect ratios, the deformation approximates uniaxial elongation, explaining the conformal advantage of line-type patterns on complex surfaces.

As illustrated in Fig. 4b, SAM can also predict conformability for various high-aspect-ratio strips on diverse surfaces. We tested strips of width $W = 3$ mm with aspect ratios from 8:1 to 25:1 on four target surfaces: a spherical surface ($R = 14$ mm), a high-curvature ellipsoid surface, a high-curvature paraboloidal surface, and a free-form surface ($L = 24$ mm, $z = 65$ mm). Results are summarized in Fig. 4c. Predictions above the red dashed line ($\lambda_{max} > \lambda_{frac.}$) correspond to fracture, as shown in Fig. 4d. Predictions between the blue and red lines ($1.00 = \lambda_{comp.} < \lambda_{min} \le \lambda_{max} \le \lambda_{frac.}$) represent compliant attachment, where Fig. 4e shows cases with internal stretching ($\lambda > \lambda_{comp.}$) and Fig. 4f shows nearly strain-free attachment ($\lambda_{min} = \lambda_{max} \approx \lambda_{comp.}$). Purple region where $\lambda_{min} < \lambda_{comp.}$ indicates compression failure, corresponding to the experimental example in Fig. 4g. Notably, for the compression case, SAM neglected interfacial adhesion and friction by setting $\alpha = 1.0$ and $\beta = 0.0$ (Supplementary Movie 3). Repeated measurements confirmed the model's accuracy across these regimes.

To demonstrate applicability in realistic electronic devices, we tested copper serpentine interconnects integrated with LEDs on a spherical surface ($R = 16$ mm) (as illustrated in Fig. 4h). Two serpentine designs were studied: one with a radius of 1400 μm ($\lambda_{comp.} = 1.00$, $\lambda_{frac.} = 1.57$) and another with 1650 μm ($\lambda_{comp.} = 1.00$, $\lambda_{frac.} = 1.19$), each comprising $n = 5$ unit cells (parameters in Supplementary Fig. S22). The target shape was the projection of the serpentine axis onto the spherical surface. For the 1400 μm design, SAM predicted $1.00 < \lambda_{min} = \lambda_{max} = 1.21 < 1.57$, indicating successful attachment and functional LEDs, which is confirmed by the experimental result shown in Fig. 4i. For the 1650 μm design, $\lambda_{max} >$ reduced $\lambda_{frac.} = 1.19$ predicted fracture and LED failure, which was also validated in Fig. 4j. The model accurately predicted both critical attachment ($95\% \lambda_{frac.} < \lambda_{max} < 100\% \lambda_{frac.}$) and critical failure ($100\% \lambda_{frac.} < \lambda_{max} < 110\% \lambda_{frac.}$) scenarios in repeated trials.

In summary, SAM not only explains the enhanced conformability of high-aspect-ratio patterns but also provides reliable quantitative predictions for diverse attachments, including serpentines, Mercator-projection cut patterns, and 3D shapes (experimental results see Supplementary Note 4, Figs. S23 and S24).

Conformability analysis and conformal design for arbitrary shape-surface mappings

Beyond predictive analysis, the model serves as a powerful tool for conformal design, that is, the inverse process of designing a planar initial pattern that, after attachment, matches a desired target pattern on a complex 3D surface. The general workflow is outlined in Fig. 5a: (i) a 3D model of the target surface is acquired (e.g., via machine vision); (ii) the surface is parameterized and SAM computes the strain distribution ($\lambda(u, v)$, with u and v as arbitrary surface parameters) for a candidate attachment; (iii) the initial coordinates (U, V) are inversely derived from the target coordinates $r(U, V)$ and the strain field using the relationship:

$$(U, V) \overset{\lambda(u,v)}{\longleftrightarrow} r(U, V) \tag{4}$$

We demonstrate this capability through three design examples of predicting and increasing complexity.

Conformal Design of a 3D Antenna Pattern (Fig. 5b and Supplementary Table S9). A spherical target surface ($R = 16$ mm) was designed with an equi-spiral antenna target pattern (6 turns, spacing is 2000 μm). The initial substrate was a PDMS circle ($D = 14$ mm), and the pattern was fabricated via spin-coating transfer[70]. For the control group (ignoring conformal mapping), the spiral exhibited severe distortion upon attachment:

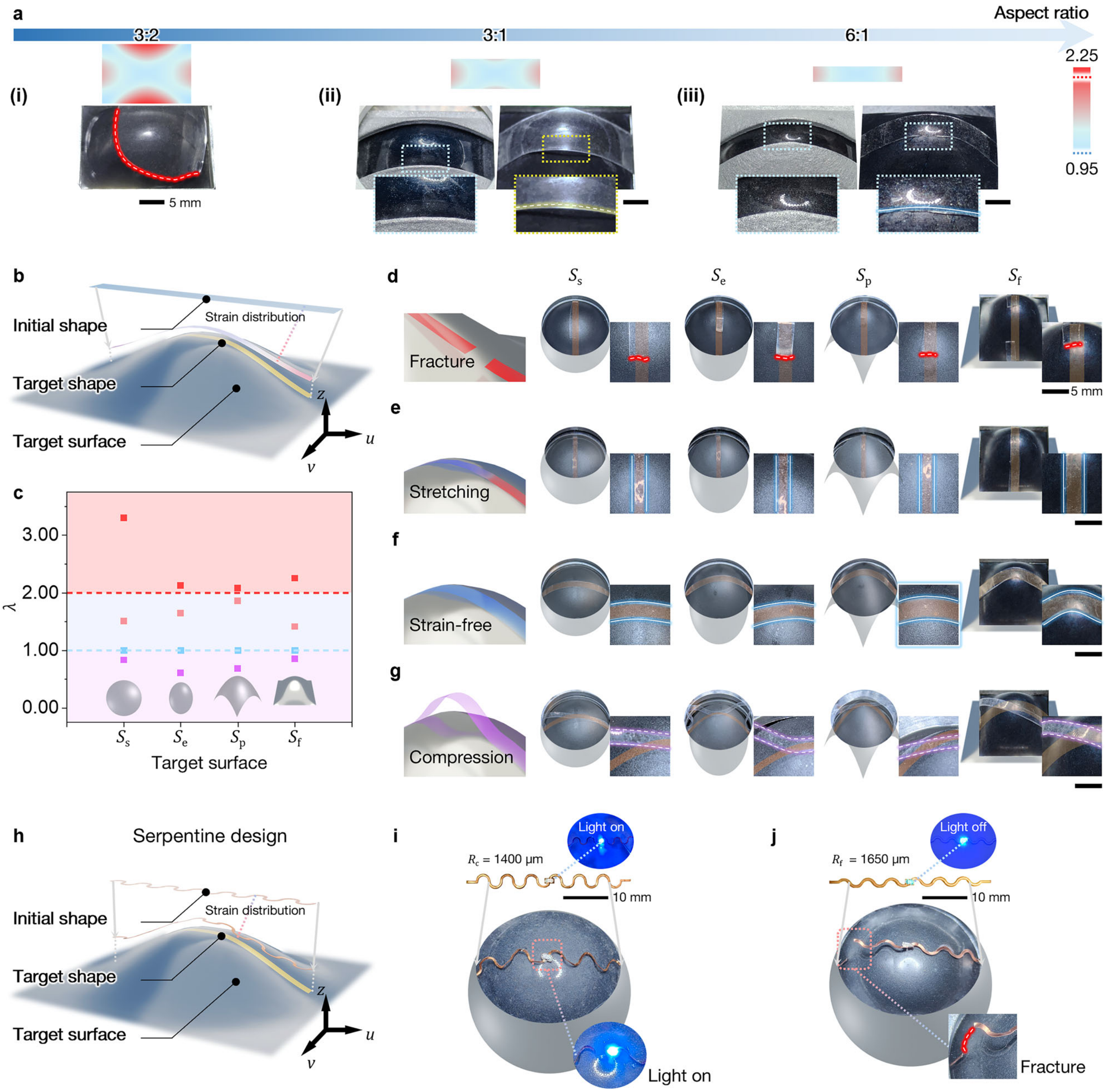

Fig. 4 | Conformability analysis and prediction for high-aspect-ratio structures. **a** Experimental validation of SAM predictions for strips with aspect ratios of 3:2, 3:1, and 6:1 on a free-form surface. **b** Schematic of a line-type device conforming to a curved surface. **c** SAM-predicted maximum elongations for different line-type shape-surface mappings, with aspect ratios from 8:1 to 25:1 on four target surfaces, including spherical, ellipsoid, paraboloidal, and free-form surfaces. Experimental examples on four surfaces corresponding to predicted regimes: **d** fracture, **e** compliant with stretch, **f** compliant without stretch, and **g** compression. **h** Schematic of a serpentine structure attachment. **i, j** Functional validation using LED-integrated serpentine interconnects: **i** successful attachment and **j** fracture failure on a spherical surface, as predicted by SAM.

spacing at the 4th turn deviated by 14.22% from target (Fig. 5c (i)), with a maximum error of 45.73% and an average error of 17.42%, as shown in Fig. 5d. In contrast, the SAM-designed precursor pattern (considering conformal mapping) yielded post-attachment spacing errors below 0.50% at the 4th turn and an average error of only 1.94% across all turns (Fig. 5c (ii), d). The model completed this design in 0.043 s, over 800 times faster than an equivalent FEA method (35 s). 2D designs of antenna patterns are illustrated in the Supplementary Fig. S25. Additional designs for equidistant points and curves (Supplementary Figs. S26 and S27, Table S10) consistently reduced errors from >12% to <2.5%, highlighting the method's precision for fabricating fine 3D electrode patterns.

Complex Multi-Parameter Pattern: A Star Map (Fig. 5e). To test scalability, we designed a star map of the northern hemisphere (120 stars, 240 coordinate parameters in Supplementary Data S3) onto a spherical "celestial" surface ($R = 20$ mm). The initial pattern was inkjet-printed with conductive silver paste on a PDMS disc ($D = 16$ mm). After conformal attachment, the spatial distribution of constellations such as Ursa Minor and the Big Dipper, shown in Fig. 5f (i), (ii), matched actual celestial charts with 99% spatial distribution similarity[71]. The entire design computation required only 0.044 s, demonstrating efficiency even for high-dimensional parameter sets.

Validation on Organ and Engineering Surfaces. Finally, we validated SAM's predictive power on highly irregular, mesh-based surfaces. On a 1:1 scale heart model, as shown in Fig. 5g, the model correctly distinguished between a conformable serpentine trace ($\lambda_{max} = 1.35 < \lambda_{frac.} = 1.57$) and a critically failing one ($\lambda_{max} = 1.35 > \lambda_{frac.} = 1.26$). Experiments confirmed

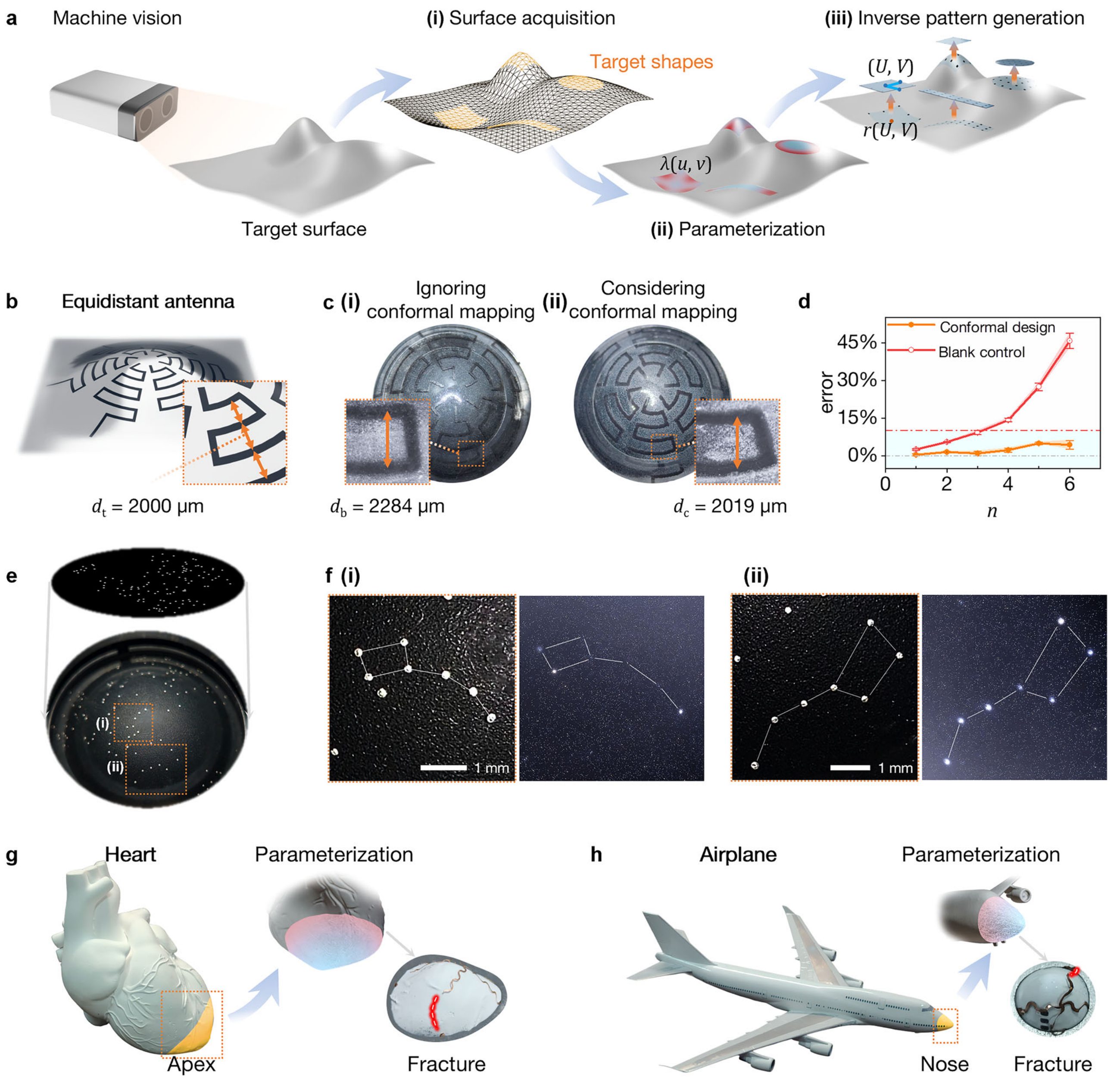

Fig. 5 | Inverse conformal design enables precise patterning on arbitrary surfaces. **a** Workflow for SAM-based conformal design: (i) Surface acquisition. (ii) Parameterization and strain computation. (iii) Inverse pattern generation. Design of a 3D equidistant antenna on a sphere: **b** Schematic of the target pattern, **c** Experimental results ignoring and considering conformal mapping, and **d** Quantitative error analysis. **e** 2D conformal design and experimental result of the star map pattern. **f** Local observation of the star map pattern: (i) Ursa Minor, (ii) The Big Dipper (Photograph by Jiacheng Liu, used with permission). Validation of conformal design for compliance on arbitrary surfaces: **g** Fracture failure on the apex of the heart. **h** Fracture failure on the nose of the aircraft.

intact attachment and fracture, respectively. Similarly, on a 1:400 aircraft nose model, SAM predicted an intermediate strain state ($\lambda_{max} = 1.30$), which lay between the failure limits of two test serpentines ($\lambda_{frac.} = 1.57$ and 1.23), again validated experimentally. Details of Serpentine-structure designs are illustrated in the Supplementary Figs. S28 and S29. Across repeated trials on arbitrary surfaces, the model maintained high accuracy, predicting both critical attachment ($90\%\lambda_{frac.} < \lambda_{max} < 100\%\lambda_{frac.}$) and critical failure ($100\%\lambda_{frac.} < \lambda_{max} < 110\%\lambda_{frac.}$) scenarios.

Discussion

Achieving predictable conformal integration of flexible electronics with complex curved surfaces remains a fundamental challenge due to the lack of a general, efficient model for predicting and designing conformal behavior. Current approaches, such as FEA, are computationally prohibitive for rapid iteration, and simplified analytical models lack generality across arbitrary geometries.

SAM achieves exceptional predictive accuracy and computational efficiency across a broad spectrum of surfaces, from canonical analytical shapes to free-form and arbitrary surfaces. This performance stems from its core formulation using the first fundamental form, which universally quantifies local metric distortion, coupled with a sliding-adhesion term that captures critical interfacial mechanics. The model not only predicts failure but also provides the first quantitative explanation for empirically observed design principles, such as the superior conformability of high-aspect-ratio serpentine traces. Although the SAM framework in this work was primarily validated using a PDMS baseline, the provided α and β coefficients remain directly applicable to other material systems with comparable mechanical and interfacial characteristics under a fixed pattern-surface geometry.

Where surface energy and friction differ by orders of magnitude from typical low-viscosity material conditions, supplementary calibration is conducted following our protocol.

Beyond prediction, SAM enables high-precision inverse conformal design. By compensating for strain-induced distortion, it allows the fabrication of complex functional patterns (e.g., antennas, sensor arrays) on 3D surfaces with placement errors reduced to below 3%. This capability bridges the gap between digital design and physical realization for curvilinear electronics.

In summary, SAM provides a unified and scalable computational framework that transforms conformal integration from a trial-and-error process into a predictable, design-led engineering discipline. It establishes a foundational tool for the development of next-generation flexible electronics in biomedical implants, conformal sensors for aerospace, and adaptive interfaces in soft robotics. The current model remains restricted to its geometric assumptions and is not suitable for high-speed dynamic scenarios, solution-coating applications, or structural bending failures within the thickness profile. Future work will extend this framework to dynamic attachment scenarios, multi-material systems, and more complex interfacial energy landscapes.

Methods

First fundamental form

An infinitesimal displacement (tangent vector) $d\vec{r}$ at any point on a curved surface $\vec{r}(u, v)$ can be expressed as follows: At a point P on the surface, there exist two natural tangent vectors:

$$\vec{r}_u = \frac{\partial \vec{r}}{\partial u}, \quad \vec{r}_v = \frac{\partial \vec{r}}{\partial v} \tag{5}$$

The infinitesimal displacement vector $d\vec{r}$ is given by:

$$d\vec{r} = \vec{r}_u du + \vec{r}_v dv \tag{6}$$

The square of the magnitude of this displacement vector $d\vec{r}$ (denoted as ds^2) is calculated via the dot product:

$$ds^2 = d\vec{r} \cdot d\vec{r} = (\vec{r}_u du + \vec{r}_v dv) \cdot (\vec{r}_u du + \vec{r}_v dv) \tag{7}$$

Expanding this expression yields the standard form of the first fundamental form:

$$I = ds^2 = Edu^2 + 2Fdudv + Gdv^2 \tag{8}$$

Here, the coefficients E, F, and G are referred to as the first fundamental coefficients, which are related to the tangent vectors through dot products:

$$E = \vec{r}_u \cdot \vec{r}_u, F = \vec{r}_u \cdot \vec{r}_v, G = \vec{r}_v \cdot \vec{r}_v \tag{9}$$

Moreover, for surface area and contact area fraction, the coefficients of the FFF (E, F, G) define the local area element dA via the square root of the metric determinant g:

$$dA = \sqrt{EG - F^2}dudv \tag{10}$$

Consequently, the total surface area A and the resulting contact area fraction Φ_{contact} to nominal surface area A_{nominal} over a domain Ω are directly formulated as:

$$A = \iint_\Omega \sqrt{EG - F^2}dudv, \quad \phi_{\text{contact}} = \frac{A}{A_{\text{nominal}}} = \frac{\iint_\Omega \sqrt{EG-F^2}dudv}{A_{\text{nominal}}} \tag{11}$$

According to Gauss's Theorema *Egregium*, the Gaussian curvature K_g is an intrinsic invariant that depends solely on the FFF components and their derivatives. It can be explicitly formulated using the Brioschi formula:

$$K_g = \frac{1}{4(EG - F^2)^2}\begin{vmatrix} E & E_v & G_u \\ F & F_v & G_v \\ G & G_v & G_u \end{vmatrix} \tag{12}$$

The global topological constraint connecting local FFF metrics to the Euler characteristic $\chi(S)$ of the conformal domain is explicitly established by integrating the intrinsic curvature and boundary geodesic curvature k_g (which is also entirely determined by the FFF):

$$\iint_S K_g\sqrt{EG - F^2}dudv + \int_{\partial S} k_g ds = 2\pi\chi(S) \tag{13}$$

For k_g, to fully resolve the boundary line integral in the Gauss-Bonnet theorem intrinsically, the geodesic curvature k_g of the thin-film boundary curve ∂S, parameterized by its arc length s as $\Gamma(s) = (u(s), v(s))$, must also be formulated strictly via the First Fundamental Form. Intrinsically, k_g is defined by the covariant acceleration of the boundary curve and can be explicitly expanded as:

$$k_g = \sqrt{g}\left(u'\left(v'' + \Gamma^2_{11}(u')^2 + 2\Gamma^2_{12}u'v' + \Gamma^2_{22}(v')^2\right) - v'\left(u'' + \Gamma^1_{11}(u')^2 + 2\Gamma^1_{12}u'v' + \Gamma^1_{22}(v')^2\right)\right) \tag{14}$$

where $u' = du/ds$, $v' = dv/ds$, $u'' = d^2u/ds^2$, and $v'' = d^2v/ds^2$ represent the kinematic derivatives along the boundary trajectory, and $g = EG\text{-}F^2$ is the metric determinant. Crucially, the Christoffel symbols of the second kind (Γ^k_{ij}) are entirely determined by the components of the First Fundamental Form (E, F, G) and their first-order partial derivatives:

$$\Gamma^k_{ij} = \frac{1}{2}g^{kl}\left(\frac{\partial g_{il}}{\partial u^j} + \frac{\partial g_{jl}}{\partial u^i} + \frac{\partial g_{ij}}{\partial u^l}\right) \tag{15}$$

where $(g_{11}, g_{12}, g_{21}, g_{22}) = (E, F, F, G)$, and g^{kl} denotes the components of the inverse metric matrix. This mathematical framework guarantees that the geodesic curvature k_g—and consequently the entire boundary energy expenditure during conformability—is explicitly and inherently encoded within the FFF of the mapped domain, requiring no extrinsic embedding data.

Above all, these explicit formulations confirm that the FFF serves as the single foundational mathematical matrix required to encode both the local strain distributions and the global topographic constraints of the target substrates.

Conformal attachment platform

A custom conformal attachment platform was constructed to mount flexible substrates of predefined initial shapes onto target surfaces (Supplementary Fig. S7). The entire system was mounted on a horizontal optical table. The platform comprised a right-angle fixing block, an initial shape mounting stage (Supplementary Fig. S7), and a target surface mounting stage, both co-mounted on the fixing block. The initial shape mounting stage consisted of: (i) a pair of gaskets to secure the flexible substrate; (ii) a clamp configuration stage holding the gaskets; and (iii) a high-precision manual translation stage to bring the initial shape into contact with the target shape.

Strain distribution measurement

Strain fields were determined by tracking microstructural marker patterns on the substrate surface via optical microscopy. A microscope was aligned along with the z-axis direction on the optical table. The marker patterns were fabricated using a photolithographic microstructure replication process, following these steps: first, a mask of the marker patterns was prepared on a silicon wafer via photolithography and wet etching; second, PDMS was spin-coated onto the wafer for replication; finally, the replicated PDMS thin film with microstructural markers was peeled off. To enhance contrast under the microscope, 0.25% black acrylic pigment was blended into the PDMS before curing, making the markers clearly visible (Supplementary Figs. S8b and S18).

Numerical methods

All runtime and mesh-related data listed in Table S7 were obtained on an AMD Ryzen 7 5800H workstation (3.20 GHz, 16.0 GB RAM). This fixed computing configuration was used uniformly for all SAM and FEA calculations to eliminate hardware-induced discrepancies in benchmark results. The finite-element-based models cover two categories: rotationally symmetric analytical surfaces and free-form surfaces.

Rotationally symmetric analytical surfaces: A 2D axisymmetric model was employed for modeling. The target surface was defined by a generatrix boundary with a specific mathematical expression, and the thin-film edges were constrained by displacement boundary conditions. The substrate was modeled as a superelastic material using a two-parameter Mooney–Rivlin constitutive law; interfacial adhesion and friction were included at the film-surface contact. Displacement-controlled loading was applied, with parameter sweeping to ensure solution convergence. Spherical cases adopt triangular meshes, whereas all remaining analytical surfaces are discretized with quadrilateral meshes. A nonlinear Fully Coupled solver was adopted with a tight relative convergence tolerance of 0.001.

Free-form surfaces: A full 3D model was employed for modeling. To reduce computational cost and improve convergence, the film boundaries were again constrained by displacement boundary conditions. The target surface was represented as the top face of a solid curved component. Physical field settings and solution procedures followed those for the analytical surfaces. Models with square or rectangular boundaries employ swept/hexahedral meshes, and tetrahedral meshes are used for other boundary configurations. A nonlinear Fully Coupled Newton-type solver was used, with the identical relative tolerance of 0.001 for convergence control.

Equidistant antennas

Equidistant antenna samples were produced by screen printing. Because the inherent tackiness of PDMS hinders direct ink deposition, a transfer-printing method was employed. A layer of release agent was first spray-coated onto the surface of a polyethylene terephthalate (PET) film. After drying, conductive carbon ink was screen-printed onto the PET using a custom mesh. PDMS was immediately spin-coated over the printed pattern, and the PDMS and conductive carbon ink were co-cured at an elevated temperature. After heating at 80 °C for 1 h, the sample was peeled from the PET, yielding a freestanding PDMS substrate with embedded carbon-ink traces.

Star map patterns

Star map patterns were fabricated by inkjet printing. The inkjet printer (model: Scientific 3) had a minimum processing resolution of 100 μm. PDMS was selected as the substrate material, and conductive silver paste served as the ink.

Data availability

All data needed to evaluate the conclusions in the paper are present in the paper and the Supplementary Materials.

Code availability

The code that supports the findings of this study is available from the corresponding author upon reasonable request.

Received: 2 April 2026; Accepted: 12 August 2026;
Published online: 19 September 2026

References

1. Shi, X. et al. Large-area display textiles integrated with functional systems. *Nature* **591**, 240–245 (2021).
2. Keum, C. et al. A substrateless, flexible, and water-resistant organic light-emitting diode. *Nat. Commun.* **11**, 6250 (2020).
3. Liu, Z., Xiang, C., Tong, Y., Li, K. H. & Guan, X. Transfer learning enhanced blood pressure monitoring based on flexible optical pulse sensing patch. *ACS Sens.* **10**, 2732–2742 (2025).
4. Zhao, H. et al. Integrated wearable sweat sensing patch for online analysis of multiple parkinson's disease-related biomarkers. *Adv. Mater.* **37**, 2504534 (2025).
5. Tang, K. W. K. et al. Bioadhesive hydrogel-coupled and miniaturized ultrasound transducer system for long-term, wearable neuromodulation. *Nat. Commun.* **16**, 4940 (2025).
6. Jin, T. et al. A wireless operated flexible bioelectronic microneedle patch for actively controlled transdermal drug delivery. *Adv. Mater.* **37**, 2417136 (2025).
7. Zhao, Q. et al. Highly stretchable and customizable microneedle electrode arrays for intramuscular electromyography. *Sci. Adv.* **10**, eadn7202 (2024).
8. Ausra, J. et al. Wireless, fully implantable cardiac stimulation and recording with on-device computation for closed-loop pacing and defibrillation. *Sci. Adv.* **8**, eabq7469 (2022).
9. Park, Y. et al. Three-dimensional, multifunctional neural interfaces for cortical spheroids and engineered assembloids. *Sci. Adv.* **7**, eabf9153 (2021).
10. Lee, W. et al. Nonthrombogenic, stretchable, active multielectrode array for electroanatomical mapping. *Sci. Adv.* **4**, eaau2426 (2018).
11. Liu, W. et al. Flexible solar cells based on foldable silicon wafers with blunted edges. *Nature* **617**, 717–723 (2023).
12. Xiong, W. et al. Bio-inspired, intelligent flexible sensing skin for multifunctional flying perception. *Nano Energy* **90**, 106550 (2021).
13. Zhao, W. et al. 2D Titanium carbide printed flexible ultrawideband monopole antenna for wireless communications. *Nat. Commun.* **14**, 278 (2023).
14. Yang, S. et al. "Cut-and-paste" manufacture of multiparametric epidermal sensor systems. *Adv. Mater.* **27**, 6423–6430 (2015).
15. Jian, W., Chen, Y. & Feng, X. 3D conformal curvy electronics: design, fabrication, and application. *ACS Nano* **19**, 15177–15188 (2025).
16. Oh, J. Y. & Bao, Z. Second skin enabled by advanced electronics. *Adv. Sci.* **6**, 1900186 (2019).
17. Chen, X. et al. Wrap-like transfer printing for three-dimensional curvy electronics. *Sci. Adv.* **9**, eadi0357 (2023).
18. Bo, R., Xu, S., Yang, Y. & Zhang, Y. Mechanically-guided 3D assembly for architected flexible electronics. *Chem. Rev.* **123**, 11137–11189 (2023).
19. Zhong, D. et al. High-speed and large-scale intrinsically stretchable integrated circuits. *Nature* **627**, 313–320 (2024).
20. Zhao, R. et al. Macromolecular engineered multifunctional room-temperature phosphorescent polymers through reversible deactivation radical polymerization. *J. Am. Chem. Soc.* **145**, 26532–26539 (2023).
21. Gao, J. et al. Ultra-robust and extensible fibrous mechanical sensors for wearable smart healthcare. *Adv. Mater.* **34**, 2107511 (2022).
22. Chen, G. et al. Strain- and strain-rate-invariant conductance in a stretchable and compressible 3D conducting polymer foam. *Matter* **1**, 205–218 (2019).
23. Tang, L., Shang, J. & Jiang, X. Multilayered electronic transfer tattoo that can enable the crease amplification effect. *Sci. Adv.* **7**, eabe3778 (2021).
24. Zhu, L., Wang, B., Handschuh-Wang, S. & Zhou, X. Liquid metal–based soft microfluidics. *Small* **16**, 1903841 (2019).
25. Liu, Z. et al. A three-dimensionally architected electronic skin mimicking human mechanosensation. *Science* **384**, 987–994 (2024).
26. Kim, B. H. et al. Three-dimensional electronic microfliers inspired by wind-dispersed seeds. *Nature* **597**, 503–510 (2021).
27. Xu, S. et al. Assembly of micro/nanomaterials into complex, three-dimensional architectures by compressive buckling. *Science* **347**, 154–159 (2015).

28. Xu, C. et al. Three-dimensional micro strain gauges as flexible, modular tactile sensors for versatile integration with micro- and macroelectronics. *Sci. Adv.* **10**, eadp6094 (2024).
29. Song, H. et al. Highly-integrated, miniaturized, stretchable electronic systems based on stacked multilayer network materials. *Sci. Adv.* **8**, eabm3785 (2022).
30. Jiang, S. et al. Soft-hinge kirigami metamaterial for self-adaptive conformal electronic armor. *Adv. Mater.* **34**, 2204091 (2022).
31. Li, X., Gai, Y., Sun, M., Li, Y. & Xu, S. Drum tower-inspired kirigami structures for rapid fabrication of multifunctional shape-memory smart devices with complex and rigid 3D geometry in a two-stage photopolymer. *Adv. Funct. Mater.* **32**, 2205842 (2022).
32. Zhao, H. et al. Buckling and twisting of advanced materials into morphable 3D mesostructures. *Proc. Natl. Acad. Sci.* **116**, 13239–13248 (2019).
33. Qian, L. et al. Self-adhesive and self-sustainable bioelectronic patch for physiological feedback electronic modulation of soft organs. *Adv. Mater.* **36**, 2406636 (2024).
34. Zhang, L. et al. Cellulose nanofiber-mediated manifold dynamic synergy enabling adhesive and photo-detachable hydrogel for self-powered E-skin. *Nat. Commun.* **15**, 3859 (2024).
35. Hao, Y. et al. A stretchable, breathable, and self-adhesive electronic skin with multimodal sensing capabilities for human-centered healthcare. *Adv. Funct. Mater.* **33**, 2303881 (2023).
36. Yang, Q. et al. Photocurable bioresorbable adhesives as functional interfaces between flexible bioelectronic devices and soft biological tissues. *Nat. Mater.* **20**, 1559–1570 (2021).
37. Ge, G. et al. Rapidly gelling, highly adhesive, and mechanically robust ionogels for stretchable and wireless electronics. *Adv. Funct. Mater.* **34**, 2310963 (2024).
38. Chen, M. et al. Crack suppression in conductive film by amyloid-like protein aggregation toward flexible device. *Adv. Mater.* **33**, 2104187 (2021).
39. Hu, H. et al. Bioinspired hierarchical structures for contact-sensible adhesives. *Adv. Funct. Mater.* **32**, 2109076 (2021).
40. Wang, L., Ha, K.-H., Rodin, G. J., Liechti, K. M. & Lu, N. Mechanics of crater-enabled soft dry adhesives: a review. *Front. Mech. Eng.* **6**, 601510 (2020).
41. Xue, Z. et al. Assembly of complex 3D structures and electronics on curved surfaces. *Sci. Adv.* **8**, eabm6922 (2022).
42. Ryu, H. et al. Transparent, compliant 3D mesostructures for precise evaluation of mechanical characteristics of organoids. *Adv. Mater.* **33**, 2100026 (2021).
43. Bae, B. et al. Stereoscopic artificial compound eyes for spatiotemporal perception in three-dimensional space. *Sci. Robot.* **9**, eadl3606 (2024).
44. Xie, Z. et al. Octopus-inspired sensorized soft arm for environmental interaction. *Sci. Robot.* **8**, eadh7852 (2023).
45. Jiang, S. et al. Flexible metamaterial electronics. *Adv. Mater.* **34**, 2200070 (2022).
46. Cheng, X. et al. Programming 3D curved mesosurfaces using microlattice designs. *Science* **379**, 1225–1232 (2023).
47. Liu, S. et al. Conformability of flexible sheets on spherical surfaces. *Sci. Adv.* **9**, eadf2709 (2023).
48. Hure, J., Roman, B. & Bico, J. Wrapping an adhesive sphere with an elastic sheet. *Phys. Rev. Lett.* **106**, 174301 (2011).
49. Hong, Y. et al. Boundary curvature guided programmable shape-morphing kirigami sheets. *Nat. Commun.* **13**, 530 (2022).
50. Jin, L., Yeager, M., Lee, Y.-J., O'Brien, D. J. & Yang, S. Shape-morphing into 3D curved surfaces with nacre-like composite architectures. *Sci. Adv.* **8**, eabq3248 (2022).
51. Hou, S. et al. Tactile-transparent wearable sensor for clinician-friendly pulse wave velocity monitoring and cardiovascular risk profiling. *ACS Nano* **19**, 32822–32835 (2025).
52. Fan, J. A. et al. Fractal design concepts for stretchable electronics. *Nat. Commun.* **5**, 3266 (2014).
53. Liu, J. et al. Self-healing kirigami assembly strategy for conformal electronics. *Adv. Funct. Mater.* **32**, 2109214 (2021).
54. Liu, W., Du, Z., Duan, Z., Li, L. & Shen, G. Neuroprosthetic contact lens enabled sensorimotor system for point-of-care monitoring and feedback of intraocular pressure. *Nat. Commun.* **15**, 5635 (2024).
55. Zhu, J. et al. *Kirigami*-inspired breathable smart contact lens for wireless monitoring of corneal hypoxia and microenvironment. *Adv. Healthc. Mater.* **14**, 2402148 (2025).
56. Yi, N. et al. Fabricating functional circuits on 3D freeform surfaces via intense pulsed light-induced zinc mass transfer. *Mater. Today* **50**, 24–34 (2021).
57. Kreyszig, E. *Introduction to Differential Geometry and Riemannian Geometry* (University of Toronto Press, 1968).
58. Yan, C., Chen, H.-Y., Lai, P.-Y. & Tong, P. Statistical laws of stick-slip friction at mesoscale. *Nat. Commun.* **14**, 6221 (2023).
59. Beer, F. P., Johnston, E. R. & DeWolf, J. T. *Mechanics of Materials* (McGraw-Hill, 2001).
60. Meitl, M. A. et al. Transfer printing by kinetic control of adhesion to an elastomeric stamp. *Nat. Mater.* **5**, 33–38 (2005).
61. Luo, Y. et al. A morphable ionic electrode based on thermogel for non-invasive hairy plant electrophysiology. *Adv. Mater.* **33**, e2007848 (2021).
62. Cheng, H. & Wang, S. Mechanics of interfacial delamination in epidermal electronics systems. *J. Appl. Mech.* **81**, 044501 (2014).
63. Box, F. et al. Delamination from an adhesive sphere: curvature-induced dewetting versus buckling. *Proc. Natl. Acad. Sci.* **120**, e2212290120 (2023).
64. Hong, I. et al. Deployable electronics with enhanced fatigue resistance for crumpling and tension. *Sci. Adv.* **11**, eadr3654 (2025).
65. Huo, X. et al. Strong and tough eutectogels with broad-range tunable mechanical properties via the hydrogen bond network-specific effect. *Adv. Funct. Mater.* **35**, 2422464 (2025).
66. Chen, X. et al. Compression-durable soft electronic circuits enabled by embedding self-healing biphasic liquid-solid metal into microstructured elastomeric channels. *Adv. Mater.* **37**, 2420469 (2025).
67. Ma, Z. et al. Controlled tough bioadhesion mediated by ultrasound. *Science* **377**, 751–755 (2022).
68. Gao, Y. et al. A universal strategy for tough adhesion of wet soft material. *Adv. Funct. Mater.* **30**, 2003207 (2020).
69. Vidler, C. et al. Dynamic interface printing. *Nature* **634**, 1096–1102 (2024).
70. Kuang, M., Wang, J., Wang, L. & Song, Y. Research progress of high-precision patterns by directly inkjet printing. *Acta Chim. Sin.* **70**, 1889–1896 (2012).
71. Zhou, W., Bovik, A. C., Sheikh, H. R. & Simoncelli, E. P. Image quality assessment: from error visibility to structural similarity. *IEEE Trans. Image Process.* **13**, 600–612 (2004).

Acknowledgements

This work was supported by the National Natural Science Foundation of China (62004166), the Natural Science Foundation of Zhejiang Province (LY23F040002), the Natural Science Foundation of Ningbo (2024J236), the National Postdoctoral Program for Innovative Talents (BX20200279), and Aeronautical Science Foundation of China (20230008053003). The authors thank Y. Li (Shanghai Zhongbin Technology Co., Ltd) for help in making the sample of star map pattern and J. Liu (Xi'an Jiaotong University) for providing the astronomical photographs of Ursa Minor and the Big Dipper.

Author contributions

Conceptualization: Q.L., Q.Z. Methodology: Q.L., Q.Z., Yuan Wei, Z.D. Investigation: Q.Z., Q.L. Visualization: Q.Z., Q.L., M.L. Funding acquisition: Q.L., Xuewen Wang, Xiaoxu Wang, W.H. Strain distribution measurement and Parameterization: Q.Z., J.S., Z.H. Sample preparation of equidistant antennas: H.M., Q.Z., Z.Z. Serpentine-structure manufacture: Q.Z., Z.W., Y.L., X.Y., Z.X. Project administration: Q.L., W.H. Supervision: Q.L., Xuewen Wang, Z.D., Xiaoxu Wang. Writing—original draft: Q. Z., Q. L., Yue Wei. Writing—review and editing: Q.L., Q.Z., Z.D.

Competing interests

W.H. is the Editor-in-Chief of npj Flexible Electronics. W.H. was not involved in the journal's review of, or decisions related to, this manuscript. Additionally, the authors declare the following patent involvements relevant to the work described in this manuscript: (1) Chinese Invention Patent No. CN202311282544.7 (Status: Granted; Applicant: Ningbo Institute of Northwestern Polytechnical University; Inventors: Q.L., Q.Z., J.S., M.L., Yuan Wei, Xuewen Wang, W.H.), which covers the conformability analysis and measurement for the construction of analytical surface SAM models; (2) Chinese Invention Patent Application No. CN202510622880.4 (Status: Pending under substantive examination; Applicant: Northwestern Polytechnical University; Inventors: Q.L., Q.Z., Yue Wei, Wukai Li, M.L., Z.W., Xiaoxu Wang, W.H.), which covers the SAM model conformability analysis and prediction related to freeform surfaces; (3) Chinese Invention Patent Application No. CN202610446800.9 (Status: Pending under substantive examination; Applicant: Northwestern Polytechnical University; Inventors: Q.L., Q.Z., Z.H., Yue Wei, M.L., Z.W., Xiaoxu Wang), which covers the SAM model conformability analysis and prediction related to mesh surfaces. The other authors declare no competing financial or non-financial interests.

Additional information

Supplementary information The online version contains supplementary material available at https://doi.org/10.1038/s41528-026-00637-2.

Correspondence and requests for materials should be addressed to Xiaoxu Wang, Xuewen Wang, Wei Huang or Qianbo Lu.